Research Article

High piezoelectricity and low strain hysteresis in PMN–PT-based piezoelectric ceramics

Jiajia Wang, Shuhao Wang, Xiang Li, Ling Li, Zhen Liu,
Ji Zhang, Yaojin Wang[*]

*School of Materials Science and Engineering, Nanjing University of Science &
Technology, Nanjing 210094, China*

© The Author(s) 2023.

Abstract: High piezoelectric properties and low strain hysteresis (*H*) are both equally necessary for practical applications in precisely controlled piezoelectric devices and systems. Unlike most of previous reports, where enhanced piezoelectric performance is typically accompanied by large hysteresis in lead-/lead-free-based ceramics, in this work, we report a reconstructed relaxor ferroelectric composition in $0.68Pb(Mg_{1/3}Nb_{2/3})O_3–0.32PbTiO_3$ (0.68PMN–0.32PT) ceramics through the introduction of $(Bi_{0.5}Na_{0.5})ZrO_3$ (BNZ) to simultaneously achieve low strain hysteresis (~7.68%), superior piezoelectricity (~1040 pC·N^{-1}), and an electric field induced strain of 0.175%. Our work not only paves the way to simultaneously large piezoelectricity and negligible strain hysteresis in ceramic systems, but also lays the foundation for the further development of novel functional materials.

Keywords: piezoelectric ceramics; dielectric; relaxor ferroelectric; strain hysteresis (*H*)

1 Introduction

Piezoelectric ceramics have historically played important roles in medical ultrasonic probes, high-density capacitors, underwater acoustic imaging systems, and micro electro mechanical systems due to their superior dielectric, ferroelectric, and piezoelectric properties [1–6]. High performance coupled with high reliability of the piezoelectric ceramics results in high demand for their use in a host of high-tech industrial applications.

Lead-based relaxor ferroelectric ceramics possess excellent electrical properties due to their compatibility of the structure, diversity of the composition, and nonuniformity of the microdomain composition, and have thus become a hotspot in condensed matter physics and material science studies. Among the relaxor ferroelectrics, $Pb(Mg_{1/3}Nb_{2/3})O_3–PbTiO_3$ (PMN–PT) is one of the most interesting candidates owing to the maturity of its preparation technology and its overall excellent performance [7–12]. As a PT end member content is increased, the density of irregular nanodomains in the ceramics also increases with the microdomains gradually merging into ferroelectric macrodomains, which shows a transition of a rhombohedral (R) relaxor ferroelectric phase to a tetragonal (T) ferroelectric phase [13]. In the proximity to R–T coexistence morphotropic phase boundary (MPB), different ferroelectric phases possess similar

energy, leading to a facilitated variation of polarization under an external stimulus, which gives rise to enhancing piezoelectric response of perovskite ferroelectrics [14,15].

The properties of the PMN–PT have been greatly improved by rare-earth element doping recently [9–11], leading to its versatile application. However, the low Curie temperature (T_C), low mechanical quality factor (Q_m), and low coercive field (E_c) reduce the temperature and electric field stability, thereby significantly limiting the use of the PMN–PT materials in high-performance piezoelectric devices. Along with high piezoelectric coefficient (d_{33}), large strain (S) and low strain hysteresis (H) are of equal importance in many piezoelectric actuator applications. One critical technical challenge is to decouple the strain and hysteresis arising from extrinsic contribution of irreversible domain wall motions [16,17]. Most ceramics or crystals possess large H in strain–electric field (S–E) curves. Although large strain ($\sim > 0.2\%$) can be achieved, there is the strain hysteresis of $> 25\%$ in $Bi_{0.5}Na_{0.5}TiO_3$-based ceramics [18–20] and also $> 15\%$ in $K_{0.5}Na_{0.5}NbO_3$-based ceramics [21–23], restricting their applications in precisely controlled devices and systems [24,25]. Compared with the lead-free ceramics, the lead-based ceramics have much smaller strain hysteresis. In Ref. [26], La-substituted lead zirconate titanate (PZT) was investigated, and the strain hysteresis as low as $\sim 4\%$ was obtained. A texture strategy can also make the strain hysteresis lower than 12% with $\sim 0.2\%$ strain [27,28]. The strain hysteresis is essentially caused by domain reorientation, where kinetics of an electric field-induced domain motion lags an input voltage. In addition to a reduction in displacement accuracy, the strain hysteresis also leads to heat and energy loss due to abrasion on domain walls [29]. Therefore, it is urgent to develop the piezoelectric ceramics with high piezoelectric properties and low-strain hysteresis simultaneously.

Heterovalent doping including both "hard" and "soft" doping to form solid solution and construct an MPB region is one of the effective methods to improve the electrical properties of the PMN–PT ceramics. References [7,9] demonstrate a progress in enhancing piezoelectric properties through the introduction of rare-earth elements into the PMN–PT ceramics, while these results are obtained at the expense of a further reduced T_C (nearly 50%). The "soft" doping promotes the domain wall movement, and the "hard" doping

plays a reverse effect [30,31]. In the lead-free piezoelectric ceramic systems, $(Bi_{0.5}Na_{0.5})ZrO_3$ (BNZ) has been widely adopted to regulate the MPB. Lv *et al*. [32] have introduced the BNZ into $(K_{0.5}Na_{0.5})NbO_3$-based ceramics and obtained a superior d_{33} of 475 pC·N^{-1}. Tao *et al*. [33] have reported an ultrahigh d_{33} of 650 pC·N^{-1} in a $(0.96{-}x)K_{0.48}Na_{0.52}Nb_{0.95}Sb_{0.05}O_3{-}$ $0.04Bi_{0.5}(Na_{0.82}K_{0.18})_{0.5}ZrO_3{-}0.4\%Fe_2O_3{-}xAgSbO_3$ system. These progresses revealed that the BNZ doping supports multiphase coexistence and enhances the strain through the promotion of domain switching and lattice distortion.

In this work, we report on a ternary system composed of a MPB composition, i.e., $0.68Pb(Mg_{1/3}Nb_{2/3})O_3{-}0.32PbTiO_3$ (0.68PMN–0.32PT), doped with the BNZ. A large d_{33} of 1040 pC·N^{-1} is obtained without a significant reduction in T_C (nearly 12%). The microstructure and dielectric response were researched, and the ferroelectric properties were also investigated. Furthermore, a large effective piezoelectric coefficient d_{33}^* along with a low H ($\sim 7.68\%$) were achieved, and the underlying mechanism for the superior performance were also addressed.

2 Experimental

$(1{-}x)(0.68Pb(Mg_{1/3}Nb_{2/3})O_3{-}0.32PbTiO_3){-}x(Bi_{0.5}Na_{0.5})$ ZrO_3 (PMN–PT–xBNZ) ceramics (x = 0.00, 0.01, 0.03, 0.05, and 0.07) were prepared by the modified columbite precursor method. PbO (99.9%), MgO (99.9%), Nb_2O_5 (99.9%), TiO_2 (99.99%), Bi_2O_3 (99.9%), Na_2CO_3 (99.99%), and ZrO_2 (99.99%) powders were dried at 120 ℃ for 12 h. A $MgNb_2O_6$ precursor was synthesized by milling for 24 h in ethanol and calcined at 1100 ℃ for 5 h. Then, PbO, $MgNb_2O_6$, and TiO_2 were weighed according to the stoichiometric ratio and mixed in ethanol for 24 h. The dried powders (PMN–PT) were sintered at 1100 ℃ for 2 h in air. Next, the PMN–PT, Bi_2O_3, Na_2CO_3, and ZrO_2 were weighed and milled again for 24 h. 7% polyvinyl alcohol was added as a binder into the dried slurry and pressed into green compacts (10 mm in diameter, 1 mm in thickness) under 10 MPa, and then heated at 600 ℃ for 2 h at a heating rate of 1.5 ℃·min^{-1}. Finally, the compacts were sintered at 1150–1200 ℃ for 2 h in air. To enable electrical characterization, the samples were sputtered with a gold film and poled under 15 kV·cm^{-1} for 20 min at 120 ℃ in oil.

Phase structures of the samples were analyzed by an X-ray diffractometer with Cu Kα radiation (D8, Bruker, Germany). The microstructure was measured by a scanning electron microscope (SEM; JSM-6700F, JEOL, Japan), and grain sizes were evaluated by the Nano Measurer software (Zhimikeji, Shanghai, China). The dielectric constant (ε_r) and dielectric loss (tanδ) were measured by an impedance analyzer (HP4294A, Agilent Technologies, USA) connected to a furnace (HF-Kejing, Hefei, China). The d_{33} was measured by a quasi-static meter (ZJ-3A, Chinese Academy of Sciences, China). A polarization–electric field (*P*–*E*) hysteresis loop and *S*–*E* curves were obtained by a ferroelectric analyzer (TF Analyzer 2000, aixACCT, Germany) at 1 Hz.

3 Results and discussion

Figure 1(a) shows X-ray diffraction (XRD) patterns of the PMN–PT–*x*BNZ ceramics at room temperature, and Fig. 1(b) shows enlarged XRD patterns in the region of 2θ = 63°–67°. It is observed that all the samples have a pure perovskite structure without any second phase, which displays a well-solid solution reaction. Obviously, split diffraction peaks of *x* = 0, e.g., the (200) peak around 2θ ≈ 45°, tend to merge into one peak, suggesting a structure transition as the addition of the BNZ. To accurately determine the effect of the BNZ doping on the phase structure evolution of the PMN–PT ceramics, Rietveld refinement with a peak profile fitted to the XRD patterns was conducted, as shown in Figs. 1(d)–1(h). For better overall refinement, the space groups of rhombohedral *R3m*, monoclinic *Pm*, and tetragonal *P4mm* were used in the calculated patterns, and the difference of the patterns showed that this matches the experimental data closely. Table 1 lists lattice parameters of the PMN–PT–*x*BNZ
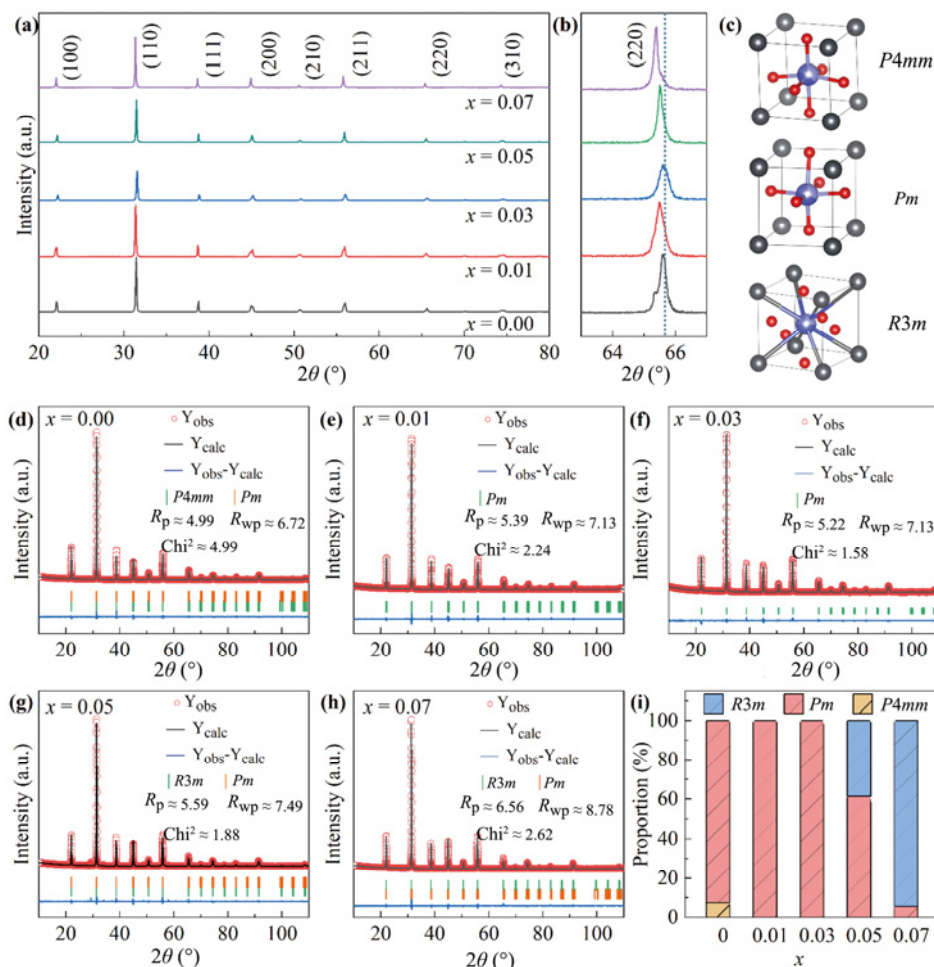

Fig. 1 (a) XRD patterns of PMN–PT–*x*BNZ ceramics measured at room temperature, (b) corresponding enlarged XRD patterns in region of 2θ = 63°–67°, (c) schematic illustrations of various polymorphs, (d–h) results of Rietveld structure refinement of ceramics, and (i) corresponding phase fractions of all ceramic samples.

Table 1 Lattice parameters of PMN–PT–*x*BNZ ceramics

Composition	Phase	*a* (Å)	*b* (Å)	*c* (Å)	*V* (Å^3)
0.00	*Pm*	4.02714	4.01265	4.03600	65.220
0.00	*P4mm*	4.01836	4.01836	4.04598	65.331
0.01	*Pm*	4.02404	4.01277	4.04143	65.259
0.03	*Pm*	4.02921	4.02159	4.04177	65.492
0.05	*Pm*	4.02796	4.02172	4.04102	65.462
0.05	*R3m*	5.69881	5.69881	6.97917	196.6809
0.07	*R3m*	5.70724	5.70724	6.99028	197.187
0.07	*Pm*	4.01630	4.02056	4.05102	65.41

ceramics, and the larger variation in cell volume leads to the XRD peaks shifting to lower diffraction angles, as shown in Fig. 1(b). It is well known that the MPB composition of the PMN–*y*PT system has been reported around *y* = 28–39 with a T phase fraction increasing with *y*, and with *P4mm* and *Pm* coexistent in the PMN–32PT [12,34]. The Rietveld refinement results revealed that the *Pm* phase is predominant (92.6%), another being the *P4mm* phase for the PMN–PT ceramics (7.4%), as shown in Fig. 1(i), and the lattice parameters are *a* = 4.027 Å, *b* = 4.013 Å, and *c* = 4.036 Å, which are consistent with those reported by other literature. With the addition of the BNZ, the phase structure tends to evolve from *Pm*–*P4mm* MPB for *x* = 0.00 to a single *Pm* phase for *x* = 0.01 and 0.03. With the continuous increase of the BNZ content, the single *Pm* phase is transformed into *R3m*–*Pm* MPB for *x* = 0.05 and 0.07. It is apparent that the overall

crystal structure presents a trend of the transformation from *Pm* to *R3m* with the introduction of the BNZ. Especially, the ceramics of *x* = 0.05 achieve relative trade-off phase coexistence of 38.55% *R3m* and 61.45% *Pm* with enhanced lattice parameters of *a* = 4.028 Å, *b* = 4.022 Å, and *c* = 4.041 Å. The reason can be attributed to that ionic substitutions of $(Bi_{0.5}Na_{0.5})^{2+}$ (~1.175 Å) for the A-site Pb^{2+} (~1.29 Å) and Zr^{4+} (~0.72 Å) for the B-site Mg^{2+} (~0.72 Å), Nb^{5+} (~0.64 Å), and Ti^{4+} (~0.61 Å) occur during the formation of the solid solution; furthermore, the size mismatch could give rise to random strain, and the valence mismatch could generate local electric fields, which lead to obvious lattice distortion and structural phase transition. It is reported that the *Pm* phase possesses only six spontaneous polarization directions along the [100] direction, while the *R3m* phase possesses eight spontaneous polarization directions along the [111] direction [35]; hence, the increase in the number of the polarization directions caused by the addition of the BNZ facilitates the reduction of a polarization barrier, which is expected to improve the dielectric and piezoelectric properties. Therefore, it is reasonable to anticipate high piezoelectric response in the PMN–PT–*x*BNZ by introducing an adequate content of the BNZ to tune the *R3m*–*Pm* phase transition temperature close to ambient environment.

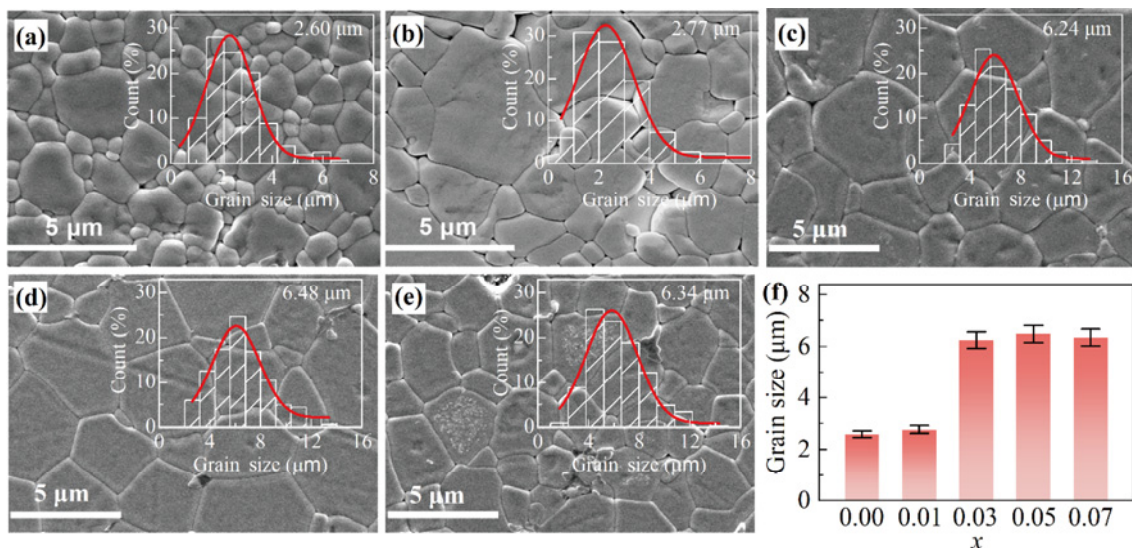Figure 2 demonstrates surface morphology images of the PMN–PT–*x*BNZ ceramics after polishing and

Fig. 2 SEM micrographs of PMN–PT–*x*BNZ ceramics; the insets show grain size distributions (calculated by Nano Measurer software) with Gaussian fitting: (a) *x* = 0.00, (b) *x* = 0.01, (c) *x* = 0.03, (d) *x* = 0.05, and (e) *x* = 0.07. (f) Grain size distributions of samples.

thermal etching. The insets of Figs. 2(a)–2(e) correspond to the grain size distribution as evaluated by the Nano Measurer software using a population of about 300 grains in SEM micrographs. All the samples show a dense, uniform microstructure with no obvious pores. With the addition of the BNZ, the average grain size shows a significant increasing trend, with a significant increase in the average grain size with the BNZ content increasing, and then keeps stable approximately with a higher dopant level. In particular, the ceramics with $x = 0.05$ show better-developed grains, as expressed by clearer grain boundaries and more uniform grain size distributions. It can be confirmed from these results that the introduction of the BNZ content into the PMN–PT can promote grain growth.

A phase transformation can be observed in temperature-dependent dielectric properties. Dielectric permittivity and loss factor of the PMN–PT–xBNZ ceramics at different frequencies and temperatures were measured and are presented in Figs. 3(a)–3(e) for various BNZ contents. The insets in Fig. 3 are linear fits between $\ln(1/\varepsilon - 1/\varepsilon_m)$ and $\ln(T - T_m)$, where γ is the slope of the fitting curves, as calculated by Eq. (1):

$$\frac{1}{\varepsilon_T} - \frac{1}{\varepsilon_m} = \frac{(T - T_m)^{\gamma}}{C} \tag{1}$$

where ε_m is the maximum dielectric constant at T_m, and C is the Curie-like constant. The γ can be used to determine a diffuseness degree, which is 1 for classical ferroelectrics and 2 for ideal relaxors [36]. The phase transition of the relaxor ferroelectrics occurs over a wide temperature range rather than a more precise T_C, as compared to that of normal ferroelectrics. For the relaxor ferroelectrics, the temperature where ε_r reaches the maximum is named T_m as an analog to T_C. The T_m and γ of the PMN–PT–xBNZ samples are summarized in Fig. 3(f). Relaxor nature of the dielectric curves is evidenced in the broad peak with respect to the temperature. The T_m of all the ceramics shift slightly higher, and the dielectric maxima broadens with the increasing frequency, consistent with γ nearly approaching 2. With the BNZ content increasing, T_m shows a decreasing trend from
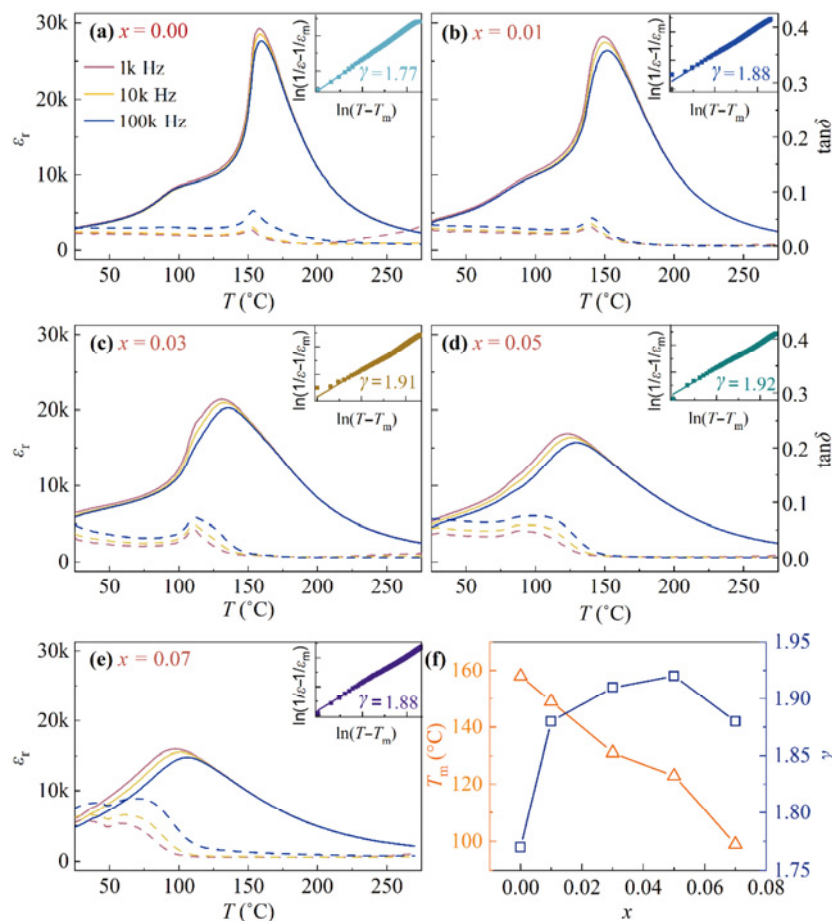

Fig. 3 (a–e) Temperature dependence of ε_r and tanδ of PMN–PT–xBNZ ceramics; the insets are graphs of $\ln(1/\varepsilon - 1/\varepsilon_m)$ vs. $\ln(T - T_m)$ for ceramics at 1 kHz. (f) T_m and γ of samples. All measured ceramics were poled.

158 ℃ for x = 0.00 to 99 ℃ for x = 0.05. According to Landau theory, T_C is directly proportional to the spontaneous polarization at 0 K (P_s) followed by Eq. (2) (α is a constant) [37,38]. In this work, Bi^{3+} and Na^+ enter the A site of the lead-based perovskites, which lower lead concentration and weaken Pb–O hybridization, leading to the decreased polarization and T_m. Meanwhile, the temperature of the R–T phase transition (T_{R-T}) broadens with the BNZ content increasing until virtually disappears. The reason may be that the phase structure is dominated by monoclinic symmetry with the space group of *Pm* and the rhombohedral with *R3m*, as suggested by the XRD data (Fig. 1).

$$T_C = \alpha P_s^2 \tag{2}$$

To explore the ferroelectric properties, the *P–E* loops and current–electric field (*J–E*) curves of the PMN–PT–xBNZ ceramics were measured at room temperature and are shown in Figs. 4(a) and 4(b), respectively. The key specifications, including remnant polarization (P_r), maximum polarization (P_{max}), coercive field (E_c), total strain (S_t), and unipolar strain (S_u), are summarized in Fig. 4(e). It can be seen clearly that all the ceramics exhibit typical ferroelectric behaviors with the saturated polarization hysteresis, while the ceramics with $0.00 \leqslant x \leqslant 0.05$ are closed to rectangular, and the ceramics with x = 0.07 tend to be thinner, indicating that the ceramics transform from the ferroelectrics to the relaxor ferroelectrics with the BNZ content increasing. The P_r and E_c values both show a downward trend by a small amount as the BNZ

content increases. This result may be contributed to more spontaneous polarization directions in a monoclinic phase than those in the T ones, and those of the R phase are between them [39]. In addition, the unit-cell distortion of the R phase would decrease due to intergranular stress constraint, which leads to the decreae of P_r, as reflected in Fig. 4(e). With the BNZ content increasing, J_{max}, corresponding to the current peak in the first quadrant, moves toward a lower electric field, which is accompanied by a decreased E_c. This indicates that it is easier to reverse the spontaneous polarization for the BNZ-modified PMN–PT ceramics. Electric field-induced strain is a crucial indicator for piezoelectric actuators [40]. The strain hysteresis properties, including S_u and bipolar strain, are characterized in Figs. 4(c) and 4(d), respectively. The S_t values of the ceramics initially decrease with the x increasing, with a local maximum at x = 0.05. The E_c value in the *P–E* loop is consistent with the minimum value in the bipolar strain. Reference [41] indicates that the T phase and R phase respond differently to an applied electric field, with high domain switching strain for the T phase and high lattice strain for the R phase.

The detailed electromechanical properties of the PMN–PT–xBNZ ceramics are listed in Table 2 wherein k_p is the planar electromechanical coupling. We can notice that the piezoelectric properties are much improved by the BNZ doping compared with those of the undoped ceramics. This result is consistent with the empirical equation (Eq. (3)), where Q_{33} is the electrostrictive
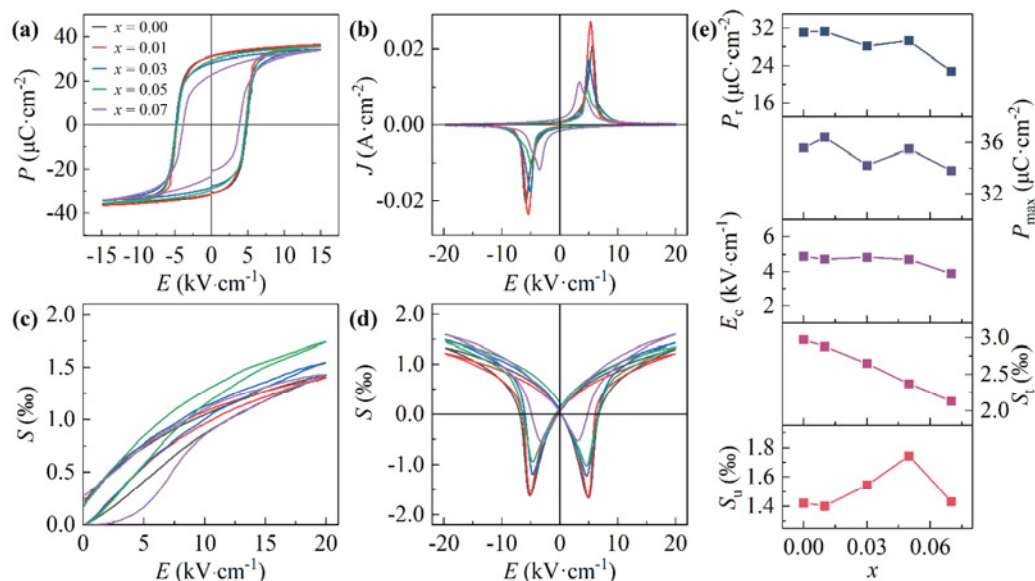

Fig. 4 Polarization and current density vs. electric field: (a) *P–E* loops and (b) *J–E* curves of PMN–PT–xBNZ ceramics. (c) Unipolar *S* and (d) bipolar *S* curves at 20 kV·cm^{-1} of samples. (e) Variation of P_r, P_{max}, E_c, S_t, and S_u as a function of BNZ content.

Table 2   Piezoelectric and dielectric properties of PMN–PT–*x*BNZ ceramics

x	d_{33} (pC·N^{-1})	d_{33}^* (pm·V^{-1})	H (%)	k_p	ε_r	tanδ	T_m (℃)
0.00	580	701	12.92	0.57	3057	0.027	158
0.01	640	712	8.56	0.58	4038	0.033	149
0.03	870	774	8.29	0.63	6559	0.042	131
0.05	1040	873	7.68	0.57	6884	0.042	123
0.07	670	716	17.55	0.38	5948	0.058	99

coefficient, which is insensitive to the phase structure of the perovskite materials [42], and ε_{33} is the dielectric permittivity.

$$d_{33} = 2Q_{33}P_r\varepsilon_{33} \tag{3}$$

To further understand the origin of the superior electrical performance of the PMN–PT–*x*BNZ ceramics, the dielectric properties and loss factors at the cryogenic temperature for the unmodified PMN–PT (the MPB region) and PMN–PT–0.05BNZ (located at the MPB, which is reconstructed and takes the highest electrical properties in this system) were measured, as shown in Figs. 5(a) and 5(b), respectively. With the temperature increasing, a large $\Delta\varepsilon_r$ of 15,062 is observed in the PMN–PT–0.05BNZ ceramics, which

is much higher than that of the undoped composition ($\Delta\varepsilon_r$ = 9067) over the measuring temperature range. For the PMN–PT–0.05BNZ, a dielectric loss peak is found though no obvious fluctuations appear in the pure PMN–PT ceramics within the same temperature range. Also, the maximum tanδ of the PMN–PT–0.05BNZ (~0.060) is much larger than that of the pure PMN–PT (~0.027). We presume that the dielectric loss peak and tanδ differences are due to the induced BNZ enhancing dynamics of local structure heterogeneity, and a similar phenomenon has been reported in Refs. [34,43,44] on Sm modification. An imaginary part of the dielectric permittivity ($\varepsilon''/\varepsilon_0$) measured within the frequency range from 1 to 30 kHz as a function of the temperature is displayed in Figs. 5(c) and 5(d). A strong dielectric relaxation behavior is observed for the doped ceramics, where T_m of $\varepsilon''/\varepsilon_0$ shifts upward by roughly 10 ℃ with the frequency increasing. This behavior is not displayed in the undoped counterpart under the same test conditions. Obviously, the addition of aliovalent BNZ will lead to the dielectric relaxor behavior of the ceramics, which could introduce random fields and enhance the structural and chemical heterogeneity on the nanoscale.
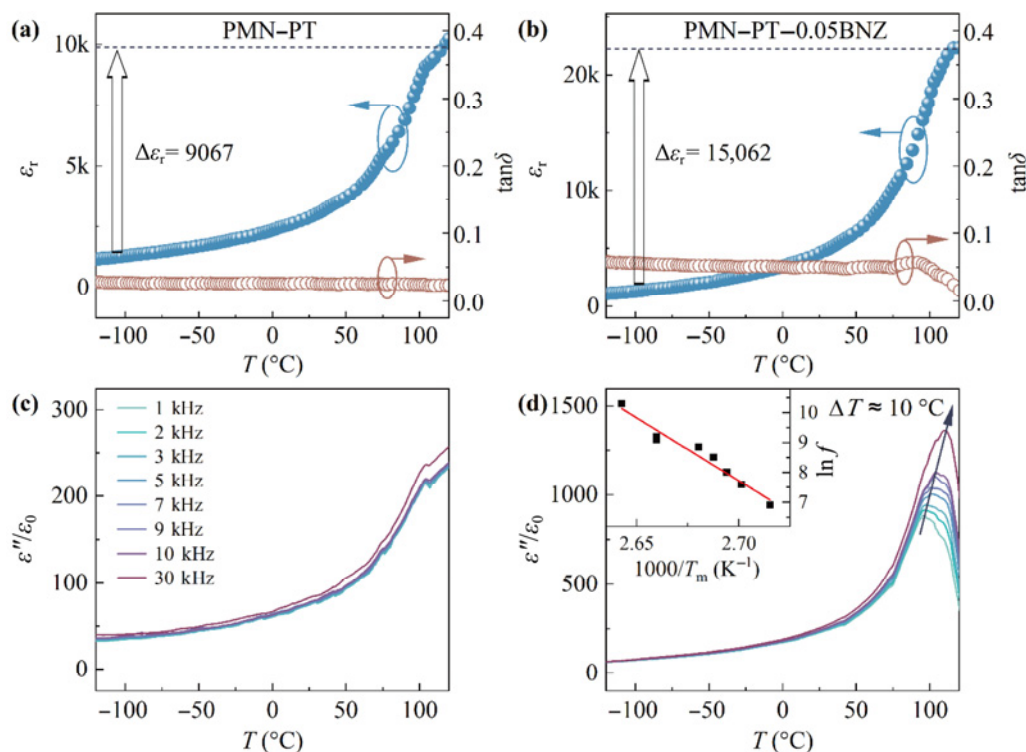

Fig. 5   Cryogenic dielectric permittivity and tanδ of (a) unmodified PMN–PT and (b) PMN–PT–0.05BNZ ceramic at 1 kHz. $\varepsilon''/\varepsilon_0$ as a function of temperature and frequency for (c) unmodified PMN–PT and (d) PMN–PT–0.05BNZ ceramic; the inset in (d) is variation of ln*f* vs. 1000/T_m for PMN–PT–0.05BNZ ceramic. Note: *f* is the measurement frequency.

To further explore the relaxor response of the BNZ-doped PMN–PT ceramics, T_m of $\varepsilon''/\varepsilon_0$ and the corresponding frequency are extracted, and the relationship between $\ln f$ and $1000/T_m$ is shown in the inset of Fig. 5(d). They follow a linear relationship and are in good agreement with Arrhenius law [45].

$$f = f_0 \exp(-E_a / (k_B T_m)) \quad (4)$$

where f_0 is the attempt frequency, and k_B is the Boltzmann constant. E_a is the activation energy [13], which is related to the volume of the local structural heterogeneity (V) and reorientating energy barrier density (ΔG, in the range of 10^5–10^7 J·m^{-3}) [46], and it is similar to those reported in Refs. [47,48], being associated with a switching energy barrier of polar nano regions (PNRs). By fitting Eq. (4), the value of E_a is calculated to be on the order of 5.84×10^{-19} J, and $\sqrt[3]{V}$, the size of the local structural heterogeneity, is then calculated and found to be in the range of 3.88–18 nm. References [13,49–51] confirm that the local structure heterogeneity on the nanoscale could flatten a local thermodynamic energy landscape and enhance the dielectric/piezoelectric response. Therefore, compared with the undoped PMN–PT ceramics, the BNZ-modified samples possess larger dielectric permittivity together with the pronounced dielectric relaxor-like behavior, which provides an evidence of the significantly enhanced piezoelectric response by the local structural heterogeneity.

Achieving high piezoelectric strain and low H are simultaneous benchmarks of high-quality materials. Figure 6(a) shows the composition dependence of d_{33}^*, d_{33}, and H. The H is calculated by Eq. (5):

$$H = \Delta S_{E_{max}/2} / S_{max} \quad (5)$$

where S_{max} is the maximum strain.

We compare the electric field-induced strain with the commercially used PZT ceramics. Figure 6(b) shows that S_{max} of ~0.175% is higher than those of the reported PZT-based ceramics [64]. In addition, the S and d_{33} values between different lead-based systems have been compared and are shown in Figs. 6(c) and 6(d), respectively. In contrast, we balance the paradox between the high d_{33} (~1040 pC·N^{-1}) and the low H (~7.68%). This work provides an appropriate compositional design for large strain with small strain hysteresis.

It states that the MPB can significantly improve the piezoelectric properties and reduce the strain hysteresis of the ceramics, which become critical factors to determine the performance of actuator devices. It has been known that the electrostrain of the piezoelectric ceramics exhibits the high strain hysteresis under a relatively high electric field due to the extrinsic contribution of the irreversible domain wall motions [17]. The dopant of the BNZ can enhance the relaxor properties by introducing the nanodomains or local
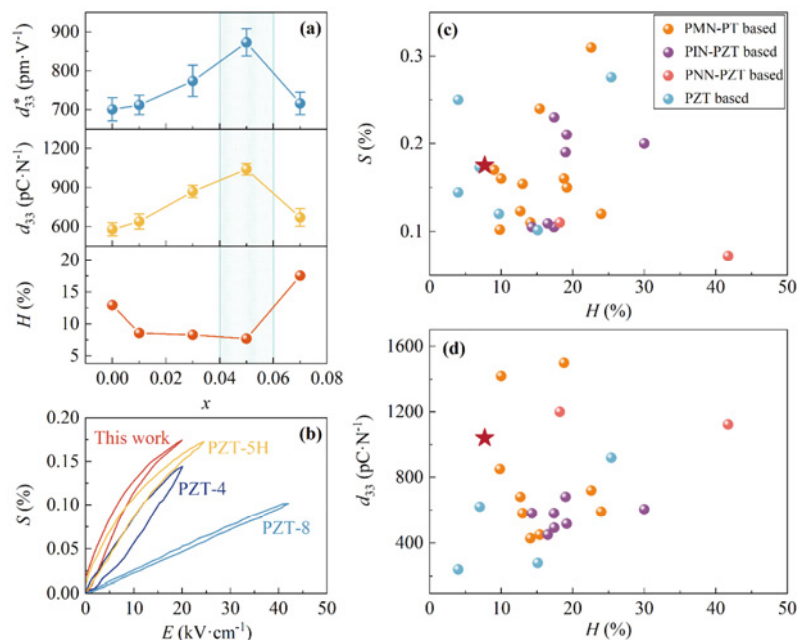

Fig. 6 (a) Composition dependence of d_{33}^*, d_{33}, and H. (b) *S–E* behavior compared between this work and commercial PZT ceramics. Comparison of this work and other well-known perovskite-structured piezoceramic systems against their (c) *H* and *S* and (d) *H* and d_{33}. These systems are compiled from Refs. [9,17,26,39,43,52–63].

heterogeneity, indicated by the dielectric performance (Fig. 3), which has been previously reported in the PMN–PT system. The improvement of the relaxor nature or local heterogeneity based on the dielectric performance agreed with neutron diffuse scattering [65]. According to Landau phenomenological theory [66], a high d_{33} can be achieved by a large value of the dielectric permittivity ($\varepsilon_{33}/\varepsilon_0$), corresponding to a flat Gibbs free energy profile with respect to the polarization. The free energy profile of the ferroelectrics can be flattened by the ferroelectric phase macroscopically [67,68] or the local structure microscopically [69,70]. As a result, the emergence of the nanodomains will reduce the irreversible domain wall motions and eventually lead to the low-strain hysteresis and high piezoelectricity.

4   Conclusions

In summary, the MPB in the PMN–PT ceramics is successfully reconstructed by doping 5% BNZ. At this composition, the electrostrain-hysteresis trade-off is achieved with the simultaneously enhanced electric field strain (~0.175%) and reduced strain hysteresis (~7.68%) while retaining the high piezoelectric property (~1040 pC·N^{-1}). Through the measurements of the phase structure, microstructure, and a series of electrical properties, we analyze the impact of dopants on the local structural heterogeneity for the relaxor ferroelectric ceramics. This study provides a referential method to achieve both piezoelectricity superior and excellent strain characteristics in the lead-based ceramics and paves a new pathway for promising application sin high-performance capacitors and high-precision actuators.

References

[1]   Yang LY, Huang HB, Xi ZZ, *et al*. Simultaneously achieving giant piezoelectricity and record coercive field enhancement in relaxor-based ferroelectric crystals. *Nat Commun* 2022, **13**: 2444.

[2]   Wu HZ, Fu SF, Wang SH, *et al*. Electrical current visualization sensor based on magneto-electrochromic effect. *Nano Energy* 2022, **98**: 107226.

[3]   Zhang Y, Jie WJ, Chen P, *et al*. Ferroelectric and piezoelectric effects on the optical process in advanced materials and devices. *Adv Mater* 2018, **30**: 1707007.

[4]   Wang Y, Wang SH, Meng YZ, *et al*. Pyro-catalysis for tooth whitening via oral temperature fluctuation. *Nat Commun* 2022, **13**: 4419.

[5]   Li ZM, Yi XY, Yang JK, *et al*. Designing artificial vibration modes of piezoelectric devices using programmable, 3D ordered structure with piezoceramic strain units. *Adv Mater* 2022, **34**: 2107236.

[6]   Li DX, Zeng XJ, Li ZP, *et al*. Progress and perspectives in dielectric energy storage ceramics. *J Adv Ceram* 2021, **10**: 675–703.

[7]   Quan Y, Ren W, Niu G, *et al*. Large piezoelectric strain with superior thermal stability and excellent fatigue resistance of lead-free potassium sodium niobate-based grain orientation-controlled ceramics. *ACS Appl Mater Interfaces* 2018, **10**: 10220–10226.

[8]   Li CC, Xu B, Lin DB, *et al*. Atomic-scale origin of ultrahigh piezoelectricity in samarium-doped PMN–PT ceramics. *Phys Rev B* 2020, **101**: 140102.

[9]   Yan PK, Qin YL, Xu ZY, *et al*. Highly transparent Eu-doped 0.72PMN–0.28PT ceramics with excellent piezoelectricity. *ACS Appl Mater Interfaces* 2021, **13**: 54210–54216.

[10] Guo QH, Hou LT, Li F, *et al*. Investigation of dielectric and piezoelectric properties in aliovalent Eu^{3+}-modified Pb(Mg$_{1/3}$Nb$_{2/3}$)O$_3$–PbTiO$_3$ ceramics. *J Am Ceram Soc* 2019, **102**: 7428–7435.

[11] Zhou S, Lin DB, Su YM, *et al*. Enhanced dielectric, ferroelectric, and optical properties in rare earth elements doped PMN–PT thin films. *J Adv Ceram* 2021, **10**: 98–107.

[12] Lu B, Jian XD, Lin XW, *et al*. Enhanced electrocaloric effect in 0.73Pb(Mg$_{1/3}$Nb$_{2/3}$)O$_3$–0.27PbTiO$_3$ single crystals via direct measurement. *Crystals* 2020, **10**: 451.

[13] Singh AK, Pandey D. Evidence for M$_B$ and M$_C$ phases in the morphotropic phase boundary region of (1−x)[Pb(Mg$_{1/3}$Nb$_{2/3}$)O$_3$]–xPbTiO$_3$: A Rietveld study. *Phys Rev B* 2003, **67**: 064102.

[14] Li F, Zhang SJ, Yang TN, *et al*. The origin of ultrahigh piezoelectricity in relaxor-ferroelectric solid solution crystals. *Nat Commun* 2016, **7**: 13807.

[15] Fan LL, Chen J, Ren Y, *et al*. Unique piezoelectric properties of the monoclinic phase in Pb(Zr,Ti)O$_3$ ceramics:

Large lattice strain and negligible domain switching. *Phys Rev Lett* 2016, **116**: 027601.

[16] Fang MX, Ji YC, Zhang Z, *et al*. Re-entrant relaxor-ferroelectric composite showing exceptional electromechanical properties. *NPG Asia Mater* 2018, **10**: 1029–1036.

[17] Xia X, Jiang XG, Zeng JT, *et al*. Critical state to achieve a giant electric field-induced strain with a low hysteresis in relaxor piezoelectric ceramics. *J Materiomics* 2021, **7**: 1143–1152.

[18] Li TY, Liu C, Shi P, *et al*. High-performance strain of lead-free relaxor-ferroelectric piezoceramics by the morphotropic phase boundary modification. *Adv Funct Materials* 2022, **32**: 2270184.

[19] Bai W, Zhao X, Ding Y, *et al*. Giant field-induced strain with low hysteresis and boosted energy storage performance under low electric field in $(Bi_{0.5}Na_{0.5})TiO_3$-based grain orientation-controlled ceramics. *Adv Electro Mater* 2020, **6**: 2000332.

[20] Cao WP, Sheng J, Qiao YL, *et al*. Optimized strain with small hysteresis and high energy-storage density in Mn-doped NBT–ST system. *J Eur Ceram Soc* 2019, **39**: 4046–4052.

[21] Huangfu G, Zeng K, Wang BQ, *et al*. Giant electric field-induced strain in lead-free piezoceramics. *Science* 2022, **378**: 1125–1130.

[22] Cen ZY, Cao FZ, Feng MY, *et al*. Simultaneously improving piezoelectric strain and temperature stability of KNN-based ceramics via defect design. *J Eur Ceram Soc* 2023, **43**: 939–946.

[23] Cen ZY, Xu Z, Li LT, *et al*. Improving the piezoelectric strain and anti-reduction properties of $K_{0.5}Na_{0.5}NbO_3$-based ceramics sintered in a reducing atmosphere. *Dalton Trans* 2021, **50**: 8851–8862.

[24] Ahn CW, Choi G, Kim IW, *et al*. Forced electrostriction by constraining polarization switching enhances the electromechanical strain properties of incipient piezoceramics. *NPG Asia Mater* 2017, **9**: e346.

[25] Jin L, Huo RJ, Guo RP, *et al*. Diffuse phase transitions and giant electrostrictive coefficients in lead-free Fe^{3+}-doped $0.5Ba(Zr_{0.2}Ti_{0.8})O_3$–$0.5(Ba_{0.7}Ca_{0.3})TiO_3$ ferroelectric ceramics. *ACS Appl Mater Interfaces* 2016, **8**: 31109–31119.

[26] Kumar A, Raju KCJ, Ryu J, *et al*. Composition dependent ferro-piezo hysteresis loops and energy density properties of mechanically activated $(Pb_{1-x}La_x)(Zr_{0.60}Ti_{0.40})O_3$ ceramics. *Appl Phys A* 2020, **126**: 175.

[27] Moriana AD, Zhang SJ. Determining the effects of $BaTiO_3$ template alignment on template grain growth of $Pb(Mg_{1/3}Nb_{2/3})O_3$–$PbTiO_3$ and effects on piezoelectric properties. *J Eur Ceram Soc* 2022, **42**: 2752–2763.

[28] Liu LJ, Yang B, Yang S, *et al*. Cu-modified $Pb(Mg_{1/3}Nb_{2/3})O_3$–$PbZrO_3$–$PbTiO_3$ textured ceramics with enhanced electromechanical properties and improved thermal stability. *J Eur Ceram Soc* 2022, **42**: 2743–2751.

[29] Hall DA, Stevenson PJ. High field dielectric behaviour of ferroelectric ceramics. *Ferroelectrics* 1999, **228**: 139–158.

[30] Chen C, Wang Y, Li ZY, *et al*. Evolution of electromechanical properties in Fe-doped $(Pb,Sr)(Zr,Ti)O_3$ piezoceramics. *J Adv Ceram* 2021, **10**: 587–595.

[31] Rawal B, Wathore NN, Praveenkumar B, *et al*. Idiosyncratic behaviour of $(Na_{0.495}K_{0.455}Li_{0.05})(Nb_{0.95}Ta_{0.05})O_3$–$La_2O_3$ ceramics: Synergistically improved thermal stability, ageing, and fatigue properties. *J Adv Ceram* 2019, **8**: 79–89.

[32] Lv X, Wu JG, Zhang XX. A new concept to enhance piezoelectricity and temperature stability in KNN ceramics. *Chem Eng J* 2020, **402**: 126215.

[33] Tao H, Wu HJ, Liu Y, *et al*. Ultrahigh performance in lead-free piezoceramics utilizing a relaxor slush polar state with multiphase coexistence. *J Am Chem Soc* 2019, **141**: 13987–13994.

[34] Li F, Lin DB, Chen ZB, *et al*. Ultrahigh piezoelectricity in ferroelectric ceramics by design. *Nat Mater* 2018, **17**: 349–354.

[35] Bokov AA, Ye ZG. Domain structure in the monoclinic *Pm* phase of $Pb(Mg_{1/3}Nb_{2/3})O_3$–$PbTiO_3$ single crystals. *J Appl Phys* 2004, **95**: 6347–6359.

[36] Uchino K, Nomura S. Critical exponents of the dielectric constants in diffused-phase-transition crystals. *Ferroelectrics* 1982, **44**: 55–61.

[37] Grinberg I, Rappe AM. Local structure and macroscopic properties in $PbMg_{1/3}Nb_{2/3}O_3$–$PbTiO_3$ and $PbZn_{1/3}Nb_{2/3}O_3$–$PbTiO_3$ solid solutions. *Phys Rev B* 2004, **70**: 220101.

[38] Abrahams SC, Kurtz SK, Jamieson PB. Atomic displacement relationship to curie temperature and spontaneous polarization in displacive ferroelectrics. *Phys Rev* 1968, **172**: 551–553.

[39] Wang HH, Ma M, Xia S, *et al*. Giant piezoelectric properties of the [110]-oriented PZT-5H single crystals grown by solid state crystal growth. *J Mater Chem C* 2023, **11**: 2664–2671.

[40] Mitrovic M, P Carman G, K Straub F. Response of piezoelectric stack actuators under combined electro-mechanical loading. *Int J Solids Struct* 2001, **38**: 4357–4374.

[41] Hinterstein M, Lee KY, Esslinger S, *et al*. Determining fundamental properties from diffraction: Electric field induced strain and piezoelectric coefficient. *Phys Rev B* 2019, **99**: 174107.

[42] Li F, Jin L, Xu Z, *et al*. Electrostrictive effect in ferroelectrics: An alternative approach to improve piezoelectricity. *Appl Phys Rev* 2014, **1**: 011103.

[43] Wang PB, Guo QH, Li F, *et al*. $Pb(In_{1/2}Nb_{1/2})O_3$–$PbZrO_3$–$PbTiO_3$ ternary ceramics with temperature-insensitive and superior piezoelectric property. *J Eur Ceram Soc* 2022, **42**: 3848–3856.

[44] Li F, Cabral MJ, Xu B, *et al*. Giant piezoelectricity of Sm-doped $Pb(Mg_{1/3}Nb_{2/3})O_3$–$PbTiO_3$ single crystals. *Science* 2019, **364**: 264–268.

[45] Li F, Zhang SJ, Xu Z, *et al*. The contributions of polar nanoregions to the dielectric and piezoelectric responses in

domain-engineered relaxor-PbTiO$_3$ crystals. *Adv Funct Mater* 2017, **27**: 1700310.

[46] Bell AJ. Calculations of dielectric properties from the superparaelectric model of relaxors. *J Phys Condens Matter* 1993, **5**: 8773–8792.

[47] Stock C, Van Eijck L, Fouquet P, *et al*. Interplay between static and dynamic polar correlations in relaxor Pb(Mg$_{1/3}$Nb$_{2/3}$)O$_3$. *Phys Rev B* 2010, **81**: 144127.

[48] Viehland D, Jang SJ, Cross LE, *et al*. Freezing of the polarization fluctuations in lead magnesium niobate relaxors. *J Appl Phys* 1990, **68**: 2916–2921.

[49] Xu GY, Wen JS, Stock C, *et al*. Phase instability induced by polar nanoregions in a relaxor ferroelectric system. *Nat Mater* 2008, **7**: 562–566.

[50] Liu H, Chen J, Huang HB, *et al*. Role of reversible phase transformation for strong piezoelectric performance at the morphotropic phase boundary. *Phys Rev Lett* 2018, **120**: 055501.

[51] Xu H, Wang B, Qi J, *et al*. Modulation of spin dynamics in Ni/Pb(Mg$_{1/3}$Nb$_{2/3}$)O$_3$–PbTiO$_3$ multiferroic heterostructure. *J Adv Ceram* 2022, **11**: 515–521.

[52] Wang DW, Cao MS, Zhang SJ. Investigation of ternary system PbHfO$_3$–PbTiO$_3$–Pb(Mg$_{1/3}$Nb$_{2/3}$)O$_3$ with morphotropic phase boundary compositions. *J Am Ceram Soc* 2012, **95**: 3220–3228.

[53] Hao MM, Fan GF, Cai W, *et al*. A quasi-linear piezoelectric strain behavior of [001] textured rhombohedral PMN–24% PT ceramic. *J Am Ceram Soc* 2020, **103**: 6226–6236.

[54] Luo NN, Zhang SJ, Li Q, *et al*. New Pb(Mg$_{1/3}$Nb$_{2/3}$)O$_3$–Pb(In$_{1/2}$Nb$_{1/2}$)O$_3$–PbZrO$_3$–PbTiO$_3$ quaternary ceramics: Morphotropic phase boundary design and electrical properties. *ACS Appl Mater Interfaces* 2016, **8**: 15506–15517.

[55] Zhu RF, Fang BJ, Zhao XY, *et al*. Enhancing piezoelectric properties of high-Curie temperature PMN–PH–PT piezoelectric ceramics by citrate method. *J Alloys Compd* 2018, **735**: 496–509.

[56] Li K, Sun EW, Zhang YC, *et al*. High piezoelectricity of Eu^{3+}-doped Pb(Mg$_{1/3}$Nb$_{2/3}$)O$_3$–0.25PbTiO$_3$ transparent ceramics. *J Mater Chem C* 2021, **9**: 2426–2436.

[57] Leng HY, Yan YK, Liu HR, *et al*. Design and development of high-power piezoelectric ceramics through integration of crystallographic texturing and acceptor-doping. *Acta Mater* 2021, **206**: 116610.

[58] Guo QH, Li F, Xia FQ, *et al*. Piezoelectric ceramics with high piezoelectricity and broad temperature usage range. *J Materiomics* 2021, **7**: 683–692.

[59] Bian L, Qi XD, Li K, *et al*. High-performance Pb(Ni$_{1/3}$Nb$_{2/3}$)O$_3$–PbZrO$_3$–PbTiO$_3$ ceramics with the triple point composition. *J Eur Ceram Soc* 2021, **41**: 6983–6990.

[60] Wei ZY, Li ZM, Yan YX, *et al*. High piezoelectric coefficient in W^{6+}-doped 0.08Pb(In$_{0.5}$Nb$_{0.5}$)O$_3$– 0.92Pb(Hf$_{0.47}$Ti$_{0.53}$)O$_3$ ceramic with enhanced thermal stability. *Ceram Int* 2021, **47**: 29392–29399.

[61] Zhao HY, Hou YD, Yu XL, *et al*. Ultra-broad temperature insensitive ceramics with large piezoelectricity by morphotropic phase boundary design. *Acta Mater* 2019, **181**: 238–248.

[62] Guo F, Zhang S, Long W, *et al*. SnO$_2$ modified PNN–PZT ceramics with ultra-high piezoelectric and dielectric properties. *Ceram Int* 2022, **48**: 23241–23248.

[63] Guo FF, Dong SS, Li K, *et al*. Synchronous improvement of piezoelectric property and temperature stability in PSN–PMN–PT ceramics by forming composites with ZnO. *J Eur Ceram Soc* 2022, **42**: 4881–4887.

[64] Park SE, Shrout TR. Ultrahigh strain and piezoelectric behavior in relaxor based ferroelectric single crystals. *J Appl Phys* 1997, **82**: 1804–1811.

[65] Krogstad MJ, Gehring PM, Rosenkranz S, *et al*. The relation of local order to material properties in relaxor ferroelectrics. *Nat Mater* 2018, **17**: 718–724.

[66] Fu H, Cohen RE. Polarization rotation mechanism for ultrahigh electromechanical response in single-crystal piezoelectrics. *Nature* 2000, **403**: 281–283.

[67] Haun MJ, Furman E, Jang SJ, *et al*. Thermodynamic theory of the lead zirconate–titanate solid solution system, Part I: Phenomenology. *Ferroelectrics* 1989, **99**: 13–25.

[68] Bellaiche L, Garcia A, Vanderbilt D. Finite-temperature properties of Pb(Zr$_{1-x}$Ti$_x$)O$_3$ alloys from first principles. *Phys Rev Lett* 2000, **84**: 5427–5430.

[69] Phelan D, Stock C, Rodriguez-Rivera JA, *et al*. Role of random electric fields in relaxors. *PNAS* 2014, **111**: 1754–1759.

[70] Manley ME, Abernathy DL, Sahul R, *et al*. Giant electromechanical coupling of relaxor ferroelectrics controlled by polar nanoregion vibrations. *Sci Adv* 2016, **2**: e1501814.